

## Spectral study of very high energy gamma rays from SS 433 with HAWC

R. ALFARO,<sup>1</sup> C. ALVAREZ<sup>2</sup>, J.C. ARTEAGA-VELÁZQUEZ,<sup>3</sup> D. AVILA ROJAS<sup>1</sup>, H.A. AYALA SOLARES<sup>4</sup>, R. BABU<sup>5</sup>,  
E. BELMONT-MORENO<sup>1</sup>, A. BERNAL,<sup>6</sup> K.S. CABALLERO-MORA<sup>2</sup>, T. CAPISTRÁN<sup>6</sup>, A. CARRAMIÑANA<sup>7</sup>,  
S. CASANOVA<sup>8</sup>, J. COTZOMI<sup>9</sup>, E. DE LA FUENTE<sup>10</sup>, D. DEPAOLI<sup>11</sup>, N. DI LALLA,<sup>12</sup> R. DIAZ HERNANDEZ<sup>7</sup>,  
B.L. DINGUS<sup>13</sup>, M.A. DUVERNOIS<sup>14</sup>, K. ENGEL<sup>15</sup>, T. ERGIN<sup>5</sup>, C. ESPINOZA<sup>1</sup>, K.L. FAN<sup>15</sup>, K. FANG<sup>14</sup>,  
N. FRAJIA<sup>6</sup>, S. FRAJIA,<sup>6</sup> J.A. GARCÍA-GONZÁLEZ<sup>16</sup>, A. GONZALEZ MUÑOZ<sup>1</sup>, M.M. GONZÁLEZ<sup>6</sup>,  
J.A. GOODMAN<sup>15</sup>, S. GROETSCH,<sup>17</sup> J.P. HARDING<sup>13</sup>, S. HERNÁNDEZ-CADENA<sup>18</sup>, I. HERZOG<sup>5</sup>, D. HUANG<sup>15</sup>,  
F. HUEYOTL-ZAHUANTITLA<sup>2</sup>, P. HÜNTEMEYER<sup>17</sup>, A. IRIARTE<sup>6</sup>, S. KAUFMANN,<sup>19</sup> A. LARA<sup>20</sup>, W.H. LEE<sup>6</sup>,  
J. LEE<sup>21</sup>, C. DE LEÓN<sup>3</sup>, H. LEÓN VARGAS<sup>1</sup>, A.L. LONGINOTTI<sup>6</sup>, G. LUIS-RAYA<sup>19</sup>, K. MALONE<sup>13</sup>,  
J. MARTÍNEZ-CASTRO<sup>22</sup>, J.A. MATTHEWS<sup>23</sup>, P. MIRANDA-ROMAGNOLI<sup>24</sup>, J.A. MONTES,<sup>6</sup> E. MORENO<sup>9</sup>,  
M. MOSTAFÁ<sup>25</sup>, L. NELLEN<sup>26</sup>, M.U. NISA<sup>5</sup>, R. NORIEGA-PAPAQUI<sup>24</sup>, Y. PÉREZ ARAUJO,<sup>1</sup>  
E.G. PÉREZ-PÉREZ<sup>19</sup>, C.D. RHO<sup>27</sup>, D. ROSA-GONZÁLEZ<sup>7</sup>, E. RUIZ-VELASCO<sup>11</sup>, H. SALAZAR<sup>9</sup>,  
A. SANDOVAL<sup>1</sup>, M. SCHNEIDER<sup>15</sup>, J. SERNA-FRANCO,<sup>1</sup> A.J. SMITH<sup>15</sup>, Y. SON<sup>21</sup>, R.W. SPRINGER<sup>28</sup>,  
O. TIBOLLA<sup>19</sup>, K. TOLLEFSON<sup>5</sup>, I. TORRES<sup>7</sup>, R. TORRES-ESCOBEDO<sup>18</sup>, R. TURNER<sup>17</sup>, F. UREÑA-MENA<sup>7</sup>,  
E. VARELA<sup>9</sup>, L. VILLASEÑOR<sup>9</sup>, X. WANG<sup>17</sup>, Z. WANG,<sup>15</sup> I.J. WATSON<sup>21</sup>, S. YU<sup>21</sup>, S. YUN-CÁRCAMO<sup>15</sup>  
AND H. ZHOU<sup>18</sup>  
(HAWC COLLABORATION)

<sup>1</sup>*Instituto de Física, Universidad Nacional Autónoma de México, Ciudad de Mexico, Mexico*

<sup>2</sup>*Universidad Autónoma de Chiapas, Tuxtla Gutiérrez, Chiapas, México*

<sup>3</sup>*Universidad Michoacana de San Nicolás de Hidalgo, Morelia, Mexico*

<sup>4</sup>*Department of Physics, Pennsylvania State University, University Park, PA, USA*

<sup>5</sup>*Department of Physics and Astronomy, Michigan State University, East Lansing, MI, USA*

<sup>6</sup>*Instituto de Astronomía, Universidad Nacional Autónoma de México, Ciudad de Mexico, Mexico*

<sup>7</sup>*Instituto Nacional de Astrofísica, óptica y Electrónica, Puebla, Mexico*

<sup>8</sup>*Institute of Nuclear Physics Polish Academy of Sciences, PL-31342 IFJ-PAN, Krakow, Poland*

<sup>9</sup>*Facultad de Ciencias Físico Matemáticas, Benemérita Universidad Autónoma de Puebla, Puebla, Mexico*

<sup>10</sup>*Departamento de Física, Centro Universitario de Ciencias Exactas e Ingenierías, Universidad de Guadalajara, Guadalajara, Mexico*

<sup>11</sup>*Max-Planck Institute for Nuclear Physics, 69117 Heidelberg, Germany*

<sup>12</sup>*Department of Physics, Stanford University: Stanford, CA 94305-4060, USA*

<sup>13</sup>*Los Alamos National Laboratory, Los Alamos, NM, USA*

<sup>14</sup>*Department of Physics, University of Wisconsin-Madison, Madison, WI, USA*

<sup>15</sup>*Department of Physics, University of Maryland, College Park, MD, USA*

<sup>16</sup>*Tecnologico de Monterrey, Escuela de Ingeniería y Ciencias, Ave. Eugenio Garza Sada 2501, Monterrey, N.L., Mexico, 64849*

<sup>17</sup>*Department of Physics, Michigan Technological University, Houghton, MI, USA*

<sup>18</sup>*Tsung-Dao Lee Institute & School of Physics and Astronomy, Shanghai Jiao Tong University, Shanghai, China*

<sup>19</sup>*Universidad Politécnica de Pachuca, Pachuca, Hgo, Mexico*

<sup>20</sup>*Instituto de Geofísica, Universidad Nacional Autónoma de México, Ciudad de Mexico, Mexico*

<sup>21</sup>*University of Seoul, Seoul, Rep. of Korea*

<sup>22</sup>*Centro de Investigación en Computación, Instituto Politécnico Nacional, México City, México.*

<sup>23</sup>*Dept of Physics and Astronomy, University of New Mexico, Albuquerque, NM, USA*

<sup>24</sup>*Universidad Autónoma del Estado de Hidalgo, Pachuca, Mexico*

<sup>25</sup>*Department of Physics, College of Science & Technology, Temple University, Philadelphia, PA 19122, USA*

<sup>26</sup>*Instituto de Ciencias Nucleares, Universidad Nacional Autónoma de Mexico, Ciudad de Mexico, Mexico*

Corresponding author: C.D. Rho  
cdr397@skku.edu

Corresponding author: Y. Son  
youngwan.son@cern.ch

Corresponding author: K. Fang  
kefang@physics.wisc.edu

<sup>27</sup>*Department of Physics, Sungkyunkwan University, Suwon 16419, South Korea*  
<sup>28</sup>*Department of Physics and Astronomy, University of Utah, Salt Lake City, UT, USA*

Submitted to ApJ

### ABSTRACT

Very-high-energy (0.1-100 TeV) gamma-ray emission was observed in HAWC data from the lobes of the microquasar SS 433, making them the first set of astrophysical jets that were resolved at TeV energies (Abeysekara et al. 2018). In this work, we update the analysis of SS 433 using 2,565 days of data from the High Altitude Water Cherenkov (HAWC) observatory. Our analysis reports the detection of a point-like source in the east lobe at a significance of  $6.6\sigma$  and in the west lobe at a significance of  $8.2\sigma$ . For each jet lobe, we localize the gamma-ray emission and identify a best-fit position. The locations are close to the X-ray emission sites “e1” and “w1” for the east and west lobes, respectively. We analyze the spectral energy distributions and find that the energy spectra of the lobes are consistent with a simple power-law  $dN/dE \propto E^\alpha$  with  $\alpha = -2.44_{-0.12}^{+0.13+0.04}$  and  $\alpha = -2.35_{-0.11}^{+0.12+0.03}$  for the east and west lobes, respectively. The maximum energy of photons from the east and west lobes reaches 56 TeV and 123 TeV, respectively. We compare our observations to various models and conclude that the very-high-energy gamma-ray emission can be produced by a population of electrons that were efficiently accelerated.

*Keywords:* Gamma-ray sources (633) — High mass x-ray binary stars (733) — Jets (870)

## 1. INTRODUCTION

SS 433, first discovered in 1977 (Stephenson & Sanduleak 1977), is a microquasar consisting of a compact object (i.e. a black hole or neutron star) that accretes matter from its massive companion star (Fabrika 2004). SS 433 is well-known for the emission from the jet interaction regions (also referred to as jet lobes) for which the jets terminate inside a nebula, W50,  $\sim 40$  pc away from the binary system (Safi-Harb & Ögelman 1997). The two jet emission regions, named “east” and “west”, have been studied in depth over the decades in radio (Geldzahler et al. 1980), X-rays (Brinkmann, W. et al. 2007; Safi-Harb & Petre 1999), and gamma rays (Abeysekara et al. 2018; Fang et al. 2020; H. E. S. S. Collaboration et al. 2024).

In 2018, the High Altitude Water Cherenkov (HAWC) observatory detected two multi-TeV gamma-ray hotspots spatially coincident with the known locations of the X-ray emission regions of SS 433 (Abeysekara et al. 2018). This discovery rekindled a series of observational campaigns that subsequently produced new results from experiments including the *Fermi* Large Area Telescope (*Fermi*-LAT; Fang et al. 2020), Nuclear Spectroscopic Telescope Array (NuSTAR; Safi-Harb et al. 2022), and High Energy Stereoscopic System (H.E.S.S.; H. E. S. S. Collaboration et al. 2024). These results have provided further information about the TeV emission regions of SS 433.

In this work, we present the updated results on the two jet lobes of SS 433. HAWC has accumulated  $\sim 1500$  days of more data compared to Abeysekara et al. (2018). With 2,565 days of data and improved data reconstruction, we perform morphological study in the region-of-interest (ROI) (Albert et al. 2024). We identify significant levels of gamma-ray emission corresponding to the east lobe and the west lobe through a blind search. The ROI is the brighter region as shown in Figure 1 (a).

In Section 2, we describe the HAWC observatory and the dataset used for the analysis. Also, we explain the source search pipeline used to identify the 6 sources found in the ROI through a blind search. In Section 3, we present the best-fit results on the SS 433 lobes and other sources found from the source search pipeline. We also show the spectra of the lobes computed with the HAWC data and the measured energy range of the observed gamma-ray photons. Finally, in Section 4, we discuss the multi-wavelength modeling of the two lobes and comparisons with the results from Abeysekara et al. (2018).

## 2. DATA AND ANALYSIS METHOD

### 2.1. Instrument and Data

HAWC is a particle sampling array designed to observe very-high-energy (VHE) gamma-ray events with energies between hundreds of GeV and hundreds of TeV. HAWC is located at an altitude of 4,100 m next

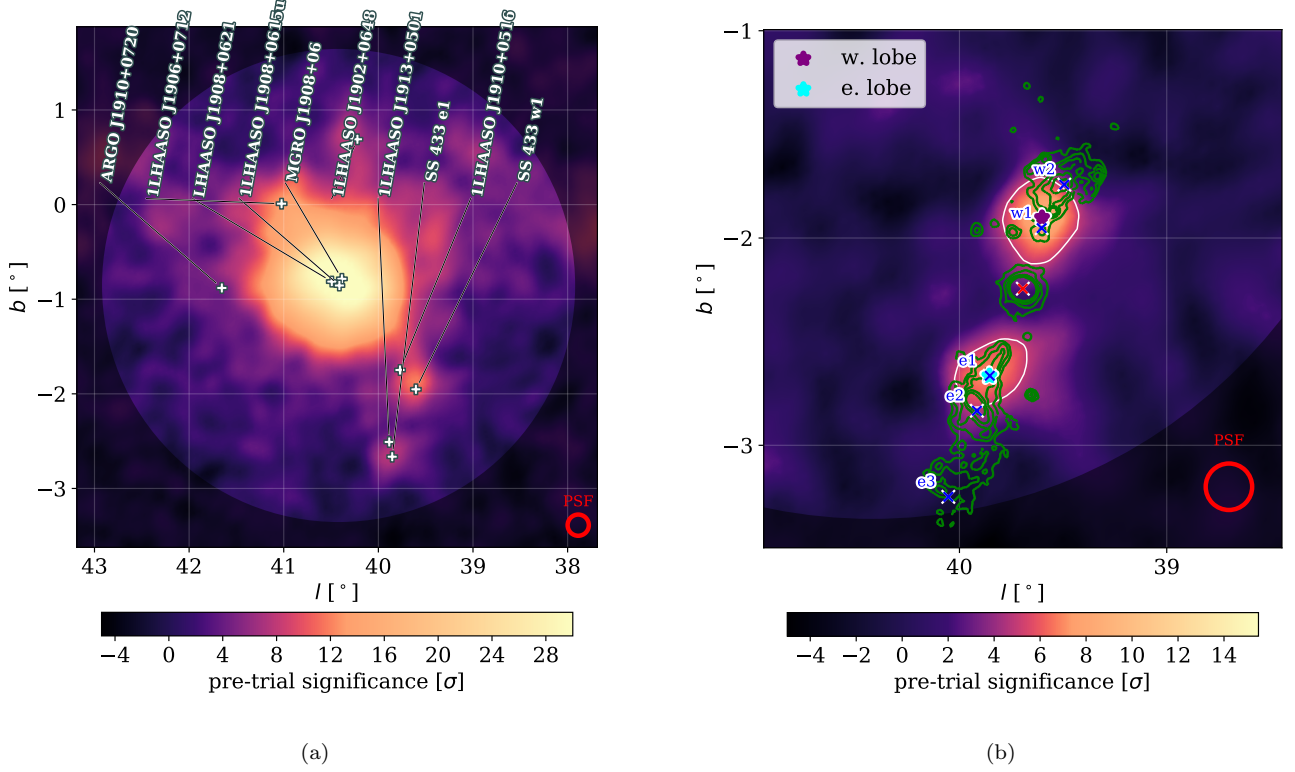


**Figure 1.** Significance maps above 1 TeV. (a) A pre-trial significance map of the SS 433 region with labels from Abdo et al. (2007); Bartoli et al. (2013); Abeysekara et al. (2018); Cao et al. (2021, 2024). (b) A pre-trial significance map zoomed in closely around SS 433. The map shows excess after the model fit but only removing background sources for the visualization of the SS 433 jet lobes. The green contour lines indicate the observational results from ROSAT (Brinkmann et al. 1996) and the white contour lines are the  $5\sigma$  contour lines as observed by this work. The X-ray emission regions “e1”, “e2”, and “e3” for the east lobe and “w1” and “w2” for the west lobe have also been indicated (Safi-Harb & Ögelman 1997). The red cross marks the known location of the binary SS 433. The purple and cyan stars indicate the best-fit locations from this work. The red ring in each panel indicates the angular resolution.

to Pico de Orizaba in Puebla, Mexico. The main array of HAWC consists of 300 water Cherenkov detectors (WCDs) providing a total geometrical area of  $\sim 220,000$  m<sup>2</sup> for indirect gamma-ray observations. Each WCD consists of a light-tight bladder containing  $\sim 200,000$  liters of purified water and four photomultiplier tubes anchored to the bottom. A WCD has a dimension of 7.3 m in diameter and 4.5 m in height that provides enough depth for the WCD to act as a calorimeter and a medium to allow air shower particles to emit Cherenkov light. HAWC has high operation time of over 95% duty cycle and a wide simultaneous field of view of 2 sr. Typically, HAWC has an event rate of  $\sim 25$  kHz of which  $\sim 0.1\%$  are gamma-ray events. More detailed information on HAWC and its operation can be found in Abeysekara et al. (2017, 2023).

Every gamma-ray event that HAWC detects is classified into an “energy bin” associated with a certain range of estimated energies (Abeysekara et al. 2019). Currently, HAWC has two energy estimation algorithms,

the ground parameter (GP) and neural network (NN) energy estimators. The GP algorithm uses the charge density at a fixed distance away from the axis of the gamma-ray air shower, while the NN algorithm uses a multilayer-perceptron architecture that employs parameters that are also used for HAWC event reconstructions (Abeysekara et al. 2019). Note that the GP and NN datasets are comparable within their uncertainties (Abeysekara et al. 2019). In this work, we have used the NN energy estimator binning scheme.

For the modeling and fitting of the sources, we use the HAWC accelerated likelihood (HAL)<sup>1</sup> plugin with the Multi-Mission Maximum Likelihood (3ML)<sup>2</sup> framework (Abeysekara et al. 2021; Vianello et al. 2015). For the source analysis, we first select a disk ROI centred at ( $l = 40.42^\circ$ ,  $b = -0.85^\circ$ ) with a radius of  $2.5^\circ$ . We then determine the number of gamma-ray sources within

<sup>1</sup> HAL; [https://github.com/threeML/hawc\\_hal](https://github.com/threeML/hawc_hal)

<sup>2</sup> 3ML; <https://github.com/threeML/threeML>

our ROI. Finally, we find for each of these sources the best spectral and morphological models by comparing a statistical measure, named test statistic (TS), defined as:

$$\text{TS} = 2 \ln \left( \frac{L_1}{L_0} \right). \quad (1)$$

In this equation, TS compares the likelihood of an alternative hypothesis ( $L_1$ ) to that of a null (background-only) hypothesis ( $L_0$ ). Analyses done with HAWC data often use TS to determine a pre-trial statistical significance of a fitted model inside a chosen ROI. The model may contain any number of free parameters depending on the number of sources and their spectral and morphological shapes being fitted. A pre-trial statistical significance measured in Gaussian standard deviation units can be estimated based on the Wilks' theorem (Wilks 1938), assuming one degree of freedom:

$$\sigma \simeq \sqrt{\text{TS}}. \quad (2)$$

Note that the Wilks' Theorem is valid for HAWC data (Abeysekara et al. 2017).

### 2.2. Source Search Pipeline

In Abeysekara et al. (2018), a point source model was fitted at each of the known X-ray emission regions “e1” and “w1” (Safi-Harb & Ögelman 1997) for the east and west jet lobes, respectively, along with an extended source model for MGRO J1908+06 at its known location. Then, a residual map was examined to confirm that the model explained the excess emission over the background. With the increased statistics in the data used for this work, we no longer use prior information about the source location or the number of sources in the region. Instead, we carry out a source search pipeline within our chosen ROI to identify the model that best describes the observational data.

We first add point sources iteratively to a baseline model until the most significant excess emission in our residual map becomes less than  $\text{TS} = 16$  Albert et al. (2023). Then, each of the point sources found in the previous step is iteratively replaced by an extended source. Each newly found model is compared with the current best model. A model that improves the fit by  $\Delta\text{TS} > 16$  is accepted as the new best model. During a successful extension test, if any of the remaining point sources become insignificant ( $\text{TS} < 16$ ), they are removed from the new best model.

Our baseline model includes a diffuse background emission (DBE) “source” fitted between  $l = 38^\circ$  and  $l = 43^\circ$ . This extended source is designed to account for unresolved sources and the Galactic diffuse emission.

The DBE is described as a source with a one dimensional Gaussian profile along the Galactic equator.

In the source search pipeline, the spectral model is assumed to be a simple power law,

$$\frac{dN}{dE_\gamma} = K \left( \frac{E_\gamma}{E_{\text{piv}}} \right)^\alpha, \quad (3)$$

where  $K$  is flux normalization at pivot energy  $E_{\text{piv}}$  and spectral index  $\alpha$ . For the pivot energy, we have used  $E_{\text{piv}} = 10$  TeV which has minimum correlation between free parameters. When an extended source is added, a Gaussian template is used to describe the spatial morphology (see Appendix A).

## 3. RESULTS

### 3.1. Significance and Morphology

Figure 1 (a) shows the map of the SS 433 region in Galactic coordinates, produced with 2,565 days of HAWC data. The color bar indicates the pre-trial significance defined in Equation 2. Known TeV gamma-ray sources in the region are labeled (Wakely & Horan 2008).

Our source search pipeline (as described in Section 2.2) finds six sources. They include one extended source HAWC J1908+0618, which corresponds to MGRO J1908+06, one point source that coincides with the east jet lobe of SS 433 and another point source that matches with the known location of the west jet lobe of SS 433. We have also found three additional point sources compared to Abeysekara et al. (2018), namely, HAWC J1902+0656, HAWC J1905+0711, and HAWC J1908+0552, resulting from the increased amount of data and the use of a full disk ROI compared to the semi-disk ROI (Abeysekara et al. 2018).

We test three different morphological models for HAWC J1908+0618, Gaussian, electron diffusion (Abeysekara et al. 2017), and inverse power law. Appendix A has the details on the morphological models.

Table 1 shows the best-fit position, flux normalization, spectral index, and TS values while assuming the simple power law spectral model (Equation 3) for each SS 433 jet lobe. Table 2 shows the best-fit parameters for the four background sources. Among these sources, HAWC J1902+0656 and HAWC J1905+0711 are reported in this work as source candidates since they have  $\text{TS} < 25$ , but they have good spatial agreement with sources from the first Large High Altitude Air Shower Observatory catalog (1LHAASO) (Cao et al. 2024). HAWC J1905+0711 has TS below 16 because while it was identified as a source in the source search pipeline, adopting an electron diffusion morphology for



Source	RA, Dec [ $^{\circ}$ , $^{\circ}$ ]	K [ $\text{TeV}^{-1}\text{cm}^{-2}\text{s}^{-1}$ ]	$\alpha$	TS
West lobe	$287.61^{+0.02}_{-0.02}$ , $5.06^{+0.02}_{-0.02}$	$2.02^{+0.32}_{-0.31} \times 10^{-15}$	$-2.35^{+0.12}_{-0.11}$	79.5
East lobe	$288.41^{+0.02}_{-0.02}$ , $4.93^{+0.02}_{-0.02}$	$1.65^{+0.28}_{-0.28} \times 10^{-15}$	$-2.44^{+0.13}_{-0.12}$	53.9

**Table 1.** Best fit results of the SS 433 lobes using point source models and simple power law spectral models (Equation 3).  $E_{\text{piv}} = 10$  TeV is used for the fit. Only the statistical uncertainties are indicated in this table.

Source (HAWC)	RA, Dec [ $^{\circ}$ , $^{\circ}$ ]	$K$ [ $\text{TeV}^{-1}\text{cm}^{-2}\text{s}^{-1}$ ]	$\alpha$	$\beta$	Extension [ $^{\circ}$ ]	TS	1LHAASO Counterpart
J1902+0656*	$285.54^{+0.03}_{-0.03}$ , $6.94^{+0.04}_{-0.03}$	$9.61^{+2.62}_{-2.53} \times 10^{-16}$	$-2.49^{+0.20}_{-0.19}$	-	-	20.0	J1902+0648
J1905+0711*	$286.46^{+0.04}_{-0.04}$ , $7.18^{+0.04}_{-0.05}$	$8.95^{+2.76}_{-2.66} \times 10^{-16}$	$-2.73^{+0.28}_{-0.27}$	-	-	12.7	J1906+0712
J1908+0552	$286.91^{+0.03}_{-0.03}$ , $5.87^{+0.03}_{-0.03}$	$1.44^{+0.35}_{-0.33} \times 10^{-15}$	$-2.19^{+0.15}_{-0.15}$	-	-	30.3	...
J1908+0618	$287.04^{+0.02}_{-0.02}$ , $6.30^{+0.01}_{-0.01}$	$9.04^{+0.48}_{-0.45} \times 10^{-14}$	$-2.42^{+0.02}_{-0.02}$	$0.18^{+0.02}_{-0.01}$	$1.54^{+0.07}_{-0.07}$	2398.9	J1908+0621

**Table 2.** Best fit results of the background sources. 1LHAASO counterparts based on their positions are indicated. Note only the statistical uncertainties are indicated here.  $\beta$  is the parameter of log parabola spectral model described in Appendix B. Note \* indicates source candidates.

HAWC J1908+0618 after the source search process has decreased its statistical significance.

Figure 1 (b) shows the significance map zoomed in around the known location of the central binary, SS 433. Note that the best-fit emission from background sources from Table 2 have been subtracted. The green contour lines are the X-ray observations from Röntgensatellit (ROSAT; Brinkmann et al. 1996), showing emissions from three distinctive regions, namely, the central binary, the west jet lobe (closer to the Galactic equator), and the east jet lobe. The crosses indicate some of the key interaction regions observed in 2-10 keV X-rays (Safi-Harb & Ögelman 1997), including “w1” and “w2” for the west jet lobe and “e1”, “e2”, and “e3” for the east jet lobe. Figure 1 (b) shows that the TeV gamma-ray hotspots are well-aligned with the X-ray jets.

The red cross at the center is the known location of the binary system. No significant emission from the central binary is detected by HAWC. The 95% confidence level upper limit on the flux of the central binary measured at 10 TeV is  $1.38 \times 10^{-15} \text{ TeV}^{-1}\text{cm}^{-2}\text{s}^{-1}$  for a spectral index of  $-2.5$ .

Figure 2 (b) shows the nested model map that contains the six sources and DBE that we have obtained as the best model for our ROI. Figure 2 (c) presents the residual map that has the final model subtracted from the HAWC significance map (Figure 2 (a)). The residual map has no obvious excess left in the ROI as expected, which is confirmed separately using a one-dimensional significance histogram.

Figure 3 shows the one-dimensional significance histogram of the residual map by collecting the significance values associated with each of the pixels within the ROI.

With all the excess fitted and subtracted, the distribution should resemble a background-only distribution. The expected background-only distribution is indicated with a red dashed curve, which is a Gaussian centered at 0 between  $-5\sigma$  and  $5\sigma$ .

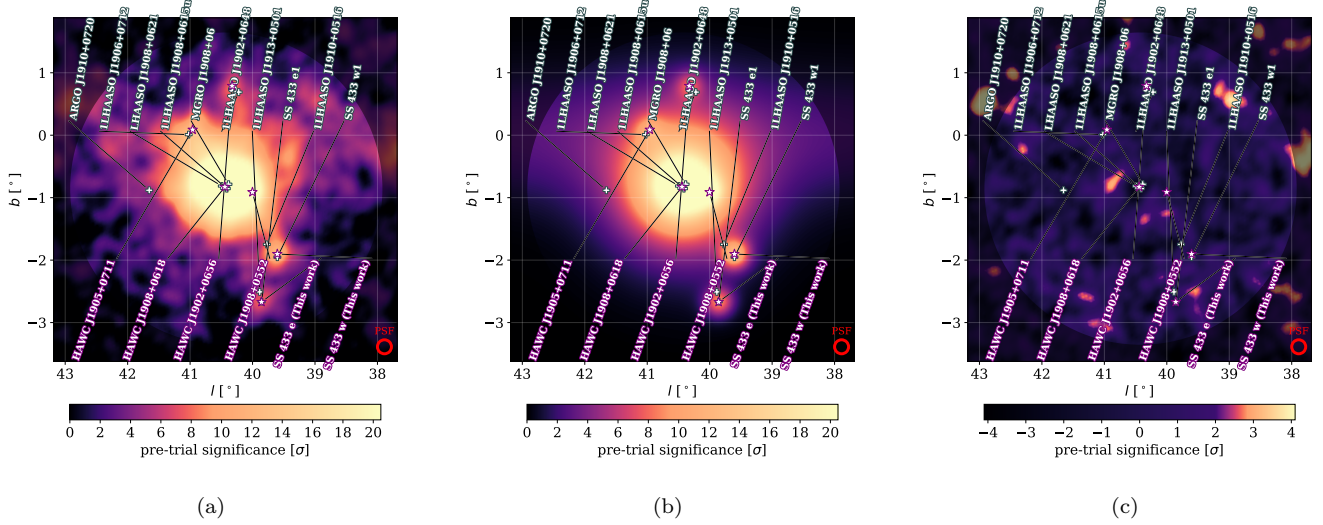
### 3.2. Spectral Studies

The newly produced HAWC dataset with improved algorithms and more statistics allows us to study the spectrum of each lobe in detail. We divide the data into 10 NN energy bins from “c” to “l” (Abeysekara et al. 2019). The true photon energy range per energy bin depends on the fitted source itself.

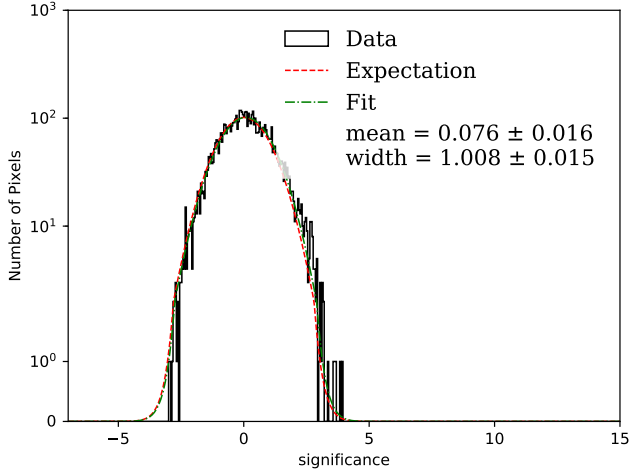
We fit a simple power-law (Equation 3) to the data corresponding to each energy bin while fixing the spectral index to the best-fit values from Table 1,  $\alpha = -2.35$  and  $\alpha = -2.44$  for the east and west lobes, respectively. Further information on the energy bins used in this work can be found in Appendix C.

Figure 4 presents the best fit spectrum of each lobe. As shown in the figure, bins “f”, “g”, “h”, and “i” are significant enough to calculate flux points for the east jet lobe, while upper limits are computed from the rest of the bins. The dotted line indicates a simple power law that is fitted to the entire energy range. As for the west jet lobe, bins “f”, “g”, “h”, “i”, and “k” have flux points. While the fitted spectrum of the east lobe is consistent with the flux point from Abeysekara et al. (2018), the fitted spectrum of the west lobe at 20 TeV is  $3\sigma$  away from the previous work. Finally, the fitted spectra of the two lobes from this work are consistent with each other.

Applying alternative spectral models for the lobes, including the cutoff power-law (COPL) and log parabola



**Figure 2.** Significance maps of the results from the source search pipeline. The lower labels indicate the sources found by this analysis. (a) HAWC data map. (b) Model map. (c) Residual map.



**Figure 3.** A one-dimensional significance histogram of the final residual map shown in Figure 2 (c).

(LP) models, do not show significant improvements to the fit, hence we conclude that the power law best describes the spectra of the two jet lobes.  $\Delta\text{TS}_{\text{COPL}} = 8$  and  $\Delta\text{TS}_{\text{LP}} = 9$ , respectively, for the east jet lobe and  $\Delta\text{TS}_{\text{COPL}} = 7$  and  $\Delta\text{TS}_{\text{LP}} = 6$ , respectively, for the west jet lobe. The description of COPL and LP can be found in Appendix B.

### 3.3. Extension and Energy Range of Jet Lobes

In this work, the SS 433 east and west jet lobes are best described using two point source models. We use the  $5\sigma$  contours to constrain the regions that produce significant VHE gamma-ray emission. Figure 1 (b) shows the  $5\sigma$  contours in white. When compared with the X-ray contours in green, we can see that the HAWC

observations are constrained to the “head” area closer to the central binary system for both of the lobes. In terms of the X-ray emission regions, both “e1” and “w1” are located close to the best-fit positions and the centers of the contours. Therefore, we confirm that the use of the known X-ray emission regions in [Abeysekara et al. \(2018\)](#) is justified.

Furthermore, we study the energy range of the gamma-ray photons observed by HAWC. The maximum photon energy at the  $1\sigma$ -level for the east lobe is 56 TeV, which is significantly higher than the maximum photon energy of 25 TeV reported in [Abeysekara et al. \(2018\)](#). The minimum photon energy at the  $1\sigma$ -level is 5 TeV. As for the west lobe, we compute the maximum photon energy to be 123 TeV and the minimum energy as 4 TeV.

### 3.4. Energy Dependent Morphologies of Jet Lobes

H.E.S.S. observed energy dependent morphological changes to the SS 433 jet lobes ([H. E. S. S. Collaboration et al. 2024](#)). We have divided our data into three energy bins to look for similar changes. Figure 5 features the significance maps corresponding to: (a)  $1 < E < 10$  TeV; (b)  $E > 10$  TeV; and (c)  $E > 18$  TeV. The maps contain contours from the H.E.S.S. observations ([H. E. S. S. Collaboration et al. 2024](#)), which are consistent with the emission observed by HAWC. While the best-fit position of the east lobe is located nearer to the central binary at higher energies, the change is smaller than the angular resolution of HAWC. We note that the emission at higher energies are clearly centered around e1 and w1 regions. Furthermore, Table 3 provides the best fit positions of the lobes for each energy

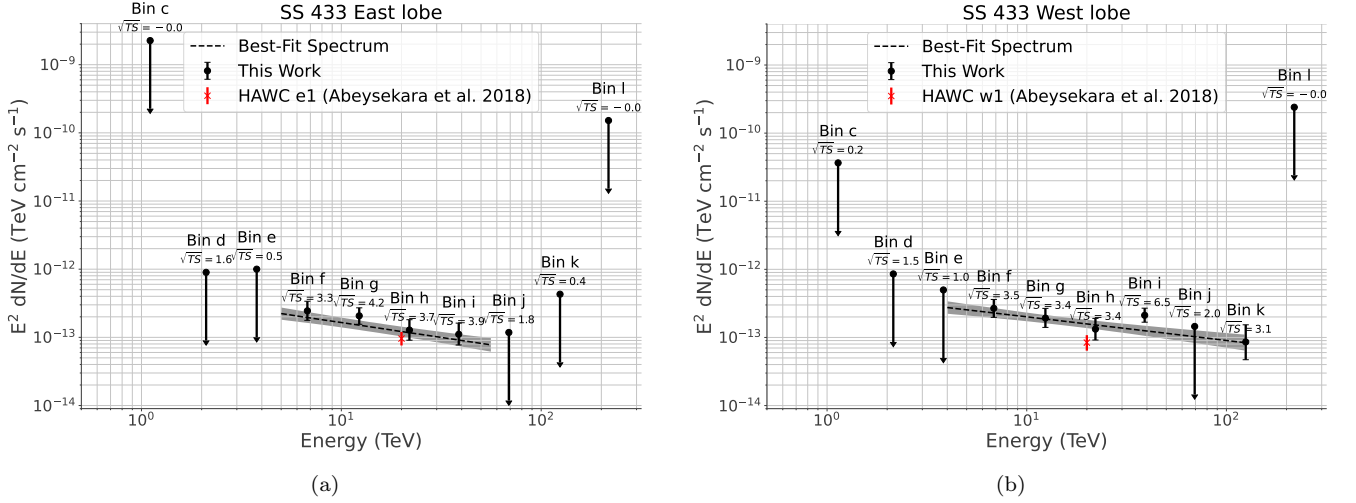


**Figure 4.** The best-fit power-law spectra of the SS 433 lobes. Information on each data point corresponding to energy bins is presented in Appendix C. The shaded region represents the  $1\sigma$  statistical error band. The red data point at 20 TeV represents the best-fit result at e1 (w1) for the east (west) lobe from [Abeysekara et al. \(2018\)](#).

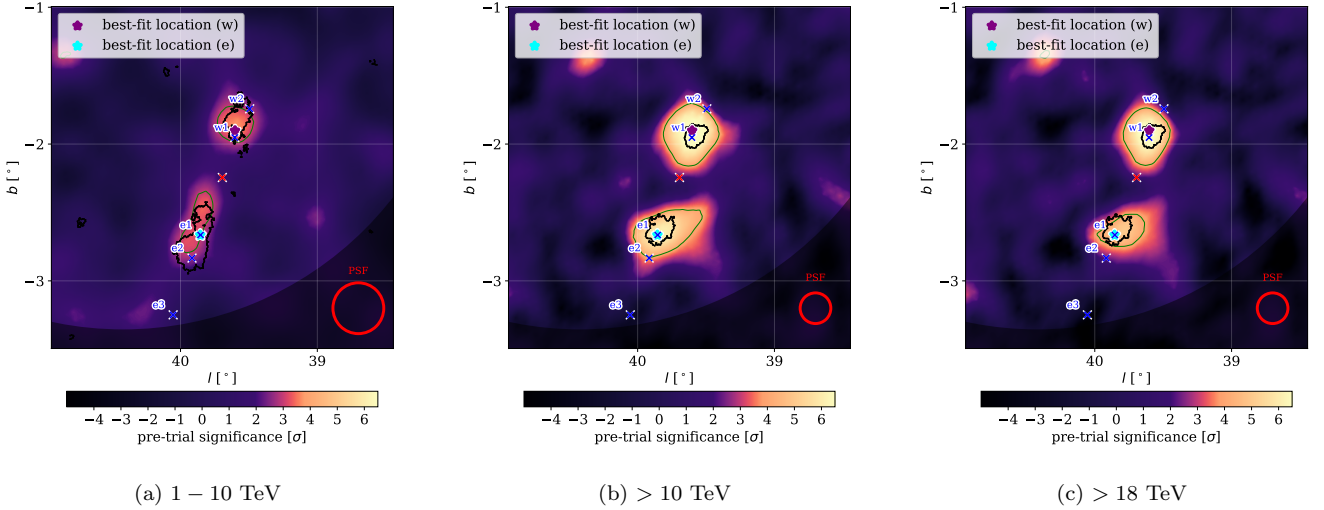


**Figure 5.** Significance maps around the SS 433 jet lobes for different energy ranges. The background sources have been subtracted. The red circle in each panel indicates the angular resolution of the bin that includes the most number of events for the given energy range. (a) shows the significance map corresponding to 1 – 10 TeV. The green contour indicates the  $3\sigma$  level in the HAWC data. The black contour indicates the  $3\sigma$  level in the H.E.S.S. data at energies 2.5 – 10 TeV. (b) shows the significance map corresponding to above 10 TeV. The green contour indicates the  $4\sigma$  level in the HAWC data at energies above 10 TeV. The black contour indicates the  $4\sigma$  level in the H.E.S.S. data at energies above 10 TeV. (c) shows the significance map corresponding to above 18 TeV. The green contour indicates the  $4\sigma$  level in the HAWC data. The black contour indicates the  $4\sigma$  level in the H.E.S.S. data at energies above 10 TeV. ([H. E. S. S. Collaboration et al. 2024](#))

Energy	West Lobe			East Lobe		
	RA	Dec	TS	RA	Dec	TS
1 – 10 TeV	$287.57 \pm 0.05$	$5.06 \pm 0.05$	15	$288.42 \pm 0.05$	$4.98 \pm 0.05$	13
> 10 TeV	$287.61 \pm 0.02$	$5.06 \pm 0.02$	70	$288.41 \pm 0.02$	$4.93 \pm 0.02$	48
> 18 TeV	$287.65 \pm 0.02$	$5.06 \pm 0.02$	60	$288.40 \pm 0.03$	$4.92 \pm 0.03$	31

**Table 3.** For each lobe, best-fit positions and TS values are presented for the energy ranges presented in Figure 5.

range. The best-fit positions computed for the lobes are consistent between the energy bins.

### 3.5. Systematic Studies

The systematic uncertainties associated with our analysis are summarized in Table 4. The systematic uncertainties contain the effects from the detector simulations (see Abeysekara et al. 2017; Abeysekara et al. 2019). The most dominant effect is the late light component, which indicates uncertainties from the discrepancy between the arrival times of light from an actual air shower and the arrival times of light from the laser pulse used for calibrations. The sources of systematic uncertainties from Table 4 are described in Abeysekara et al. (2019) in more detail.

#### 4. DISCUSSION AND CONCLUSION

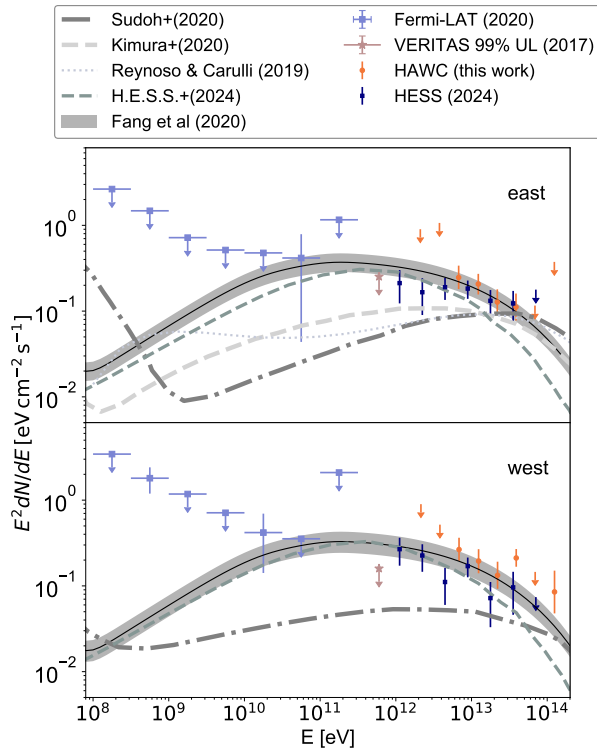


**Figure 6.** The spectral energy distribution of the gamma-ray emission site in the SS 433 east (top) and west (bottom) lobes measured by HAWC (this work; orange), *Fermi*-LAT (Fang et al. 2020, light blue markers), H.E.S.S. (H. E. S. S. Collaboration et al. 2024, navy square markers), and VERITAS (Kar 2017, brown upper limit). Models are shown for reference, including Reynoso & Carulli (2019) (parameter 3a; light grey dotted curve), Sudoh et al. (2020) (dark grey dash-dotted curves), Fang et al. (2020) (grey shaded regions), Kimura et al. (2020) (scenario D; light grey dashed curve), and H. E. S. S. Collaboration et al. (2024) (grey dashed curve).

We have analyzed 2,565 days of HAWC data to study the TeV gamma-ray emission from the jet lobes of

SS 433. The new data contain more and improved statistics to carry out a thorough blind search of the region. Our blind search successfully identifies two point sources located close to the X-ray hotspots, “e1” and “w1”, which are known as jet interaction regions for the east and west jet lobes, respectively. However, we find no evidence of extended emission for the lobes. The blind search within the ROI has also identified four background sources of which HAWC J1908+0618 is the only extended source that is best described by the electron diffusion morphological model, similar to Abeysekara et al. (2018).

Our spectral studies find that the sources can be described by a power law spectrum with no cut off. The  $1\sigma$  bound of the maximum photon energy has increased from 25 TeV to 56 TeV and 123 TeV for the east and west jet lobes, respectively, compared to our previous analysis (Abeysekara et al. 2018). The spectra are measured to be softer than previously assumed in Abeysekara et al. (2018).

When fitting to the broadband energy spectrum using an electron spectrum that follows a power-law with an exponential cutoff as in Abeysekara et al. (2018), we find the total energy of injected electrons as  $W_e = 1.3 \times 10^{47}$  erg, well within the energy budget of the kinetic power of the jets (Fabrika 2004).

The spectra in Figure 4 constructed from fitting the data that are divided into NN energy bins are consistent with the flux points at 20 TeV from Abeysekara et al. (2018). The best-fit spectral indices  $\alpha = -2.44^{+0.13}_{-0.12}$  and  $\alpha = -2.35^{+0.12}_{-0.11}$  are lower than what we assumed in Abeysekara et al. (2018) for which the spectral indices were fixed to  $\alpha = -2.0$ . The pivot energy used in this work,  $E_{\text{piv}} = 10$  TeV, is also lower than  $E_{\text{piv}} = 20$  TeV used in Abeysekara et al. (2018).

Figure 6 presents the spectral energy distribution of the gamma-ray emission from the eastern and western SS 433 jet lobes between 0.1 GeV and 100 TeV. Models have been proposed to explain the TeV emission by SS 433, invoking continuous or instantaneous injections of electrons and protons from the synchrotron knots (Reynoso & Carulli 2019; Sudoh et al. 2020; Fang et al. 2020), as well as a standing shock in the outer jets (H. E. S. S. Collaboration et al. 2024). When comparing our observation with these recent models, we find that the models confined by previous IACT limits are generally too low to explain the HAWC and H.E.S.S. observations. The grey shaded region in the figure corresponds to the best-fit gamma-ray model in Fang et al. (2020) obtained by fitting a steady electron injection model as in Abeysekara et al. (2018) to the *Fermi*-LAT and HAWC data from Abeysekara et al. (2018). The grey dashed



Type	RA, Dec [ $^{\circ}$ , $^{\circ}$ ]		Flux Normalization [ $10^{-16}$ TeV $^{-1}$ cm $^{-2}$ s $^{-1}$ ]		$\alpha$	
	west	east	west	east	west	east
Late light	$\pm 0.001, \pm 0.0007$	$\pm 0.0006, \pm 0.0008$	$\pm 1.84$	$\pm 1.55$	$\pm 0.01$	$\pm 0.02$
Charge uncertainty	$\pm 0.001, \pm 0.002$	$\pm 0.0003, \pm 0.002$	$\pm 1.06$	$\pm 0.73$	$\pm 0.01$	$\pm 0.02$
PMT threshold	$\pm 0.0002, \pm 0.0002$	$\pm 0.0006, \pm 0.0002$	$\pm 0.53$	$\pm 0.34$	$\pm 0.005$	$\pm 0.006$
PMT efficiency	$\pm 0.0005, \pm 0.002$	$\pm 0.0008, \pm 0.001$	$\pm 0.35$	$\pm 0.50$	$\pm 0.02$	$\pm 0.02$
<b>Quadratic Sum</b>	$\pm 0.002, \pm 0.003$	$\pm 0.001, \pm 0.002$	$\pm 2.22$	$\pm 1.82$	$\pm 0.03$	$\pm 0.04$

**Table 4.** Detector systematic effects measured for four different categories and their quadratic sums.

curve is a model from [H. E. S. S. Collaboration et al. \(2024\)](#) obtained by fitting a similar electron injection model to the H.E.S.S. and X-ray data. The model is in tension with the HAWC measurements above  $\sim 30$  TeV, suggesting that the multi-wavelength production mechanism may be more complicated than a one-zone model where electrons simultaneously produce X-ray and TeV gamma-ray emission.

The successful identification of SS 433 through a blind search with the HAWC data confirms the existence of gamma-ray emission by the microquasar and pinpoints the gamma-ray production sites inside the large-scale jet. The photon energy reaches beyond 100 TeV, suggesting that electrons must have been efficiently accelerated given the short cooling time at such extreme energies ([Abeysekara et al. 2018](#); [Fang et al. 2020](#)). More discoveries of very-high-energy gamma-ray-emitting jets by future air shower gamma-ray detectors will help understand the mechanism of particle acceleration at large distances from the compact object.

## 5. ACKNOWLEDGEMENTS

We acknowledge the support from: the US National Science Foundation (NSF); the US Department of Energy Office of High-Energy Physics; the Laboratory Directed Research and Development (LDRD) program of Los Alamos National Laboratory; Consejo Nacional de Ciencia y Tecnología (CONACyT), México, grants 271051, 232656, 260378, 179588, 254964, 258865, 243290, 132197, A1-S-46288, A1-S-22784, CF-2023-I-645, cátedras 873, 1563, 341, 323, Red HAWC, México; DGAPA-UNAM grants IG101323, IN111716-3, IN111419, IA102019, IN106521, IN114924, IN110521, IN102223; VIEP-BUAP; PIFI 2012, 2013, PROFOCIE

2014, 2015; the University of Wisconsin Alumni Research Foundation; the Institute of Geophysics, Planetary Physics, and Signatures at Los Alamos National Laboratory; Polish Science Centre grant, DEC-2017/27/B/ST9/02272; Coordinación de la Investigación Científica de la Universidad Michoacana; Royal Society - Newton Advanced Fellowship 180385; Generalitat Valenciana, grant CIDEAGENT/2018/034; The Program Management Unit for Human Resources & Institutional Development, Research and Innovation, NXPO (grant number B16F630069); Coordinación General Académica e Innovación (CGAI-UdeG), PRODEP-SEP UDG-CA-499; Institute of Cosmic Ray Research (ICRR), University of Tokyo; National Research Foundation of Korea (RS-2023-00280210, NRF-2021R1A2C1094974). H.F. acknowledges support by NASA under award number 80GSFC21M0002. We also acknowledge the significant contributions over many years of Stefan Westerhoff, Gaurang Yodh and Arnulfo Zepeda Domínguez, all deceased members of the HAWC collaboration. Thanks to Scott Delay, Luciano Díaz and Eduardo Murrieta for technical support.

C.D. Rho analyzed the data and prepared the original manuscript. Y. Son analyzed the data and performed the maximum likelihood analysis. K. Fang carried out the interpretation of results and the discussion section calculations. The full HAWC collaboration has contributed through the construction, calibration, and operation of the detector, the development and maintenance of reconstruction and analysis software, and vetting of the analysis presented in this manuscript. All authors have reviewed, discussed, and commented on the results and the manuscript.

## APPENDIX

### A. EXTENDED MORPHOLOGICAL MODELS

Three morphological models (Gaussian, Inverse power law, Diffusion) are tested for the modeling of the extended source HAWC J1908+0618, which is a counterpart of MGRO J1908+06. The mentioned morphological models were also tested for the modeling of MGRO J1908+06 in [Abeysekara et al. \(2018\)](#). Detailed implementation of the models

can be found in *astromodels*<sup>3</sup>. Astromodels is a Python package containing source definitions that is used with 3ML. Using the data in our ROI, we select the best model based on the relative  $\Delta\text{BIC}$  (Bayesian information criterion) obtained from the likelihood fits (Kass & Raftery 1995).

The Gaussian morphological model is described using

$$\frac{dN}{d\Omega} = \frac{1}{2\pi\sigma^2} \exp\left(-\frac{\theta^2}{2\sigma^2}\right), \quad (\text{A1})$$

where  $\theta$  is angular distance and  $\sigma$  is Gaussian width that represents the size of the fitted extended source in degrees.

The inverse power law morphological model is given by

$$\frac{dN}{d\Omega} = \left[ \pi r_{\min}^{2+\alpha} + \frac{2\pi}{(2+\alpha)} (r_{\max}^{2+\alpha} - r_{\min}^{2+\alpha}) \right]^{-1} r^\alpha, \quad (\text{A2})$$

where  $r_{\min} \leq \theta < r_{\max}$ .  $\Delta\text{BIC}$  for the inverse power law model is found to be +159.

The diffusion morphological model describes  $\gamma$ -ray emission by inverse Compton scattering of diffused electrons and positrons as

$$\frac{dN}{d\Omega} = \frac{1.22}{\pi^{3/2}\theta_d (\theta + 0.06\theta_d)} \exp\left(-\frac{\theta^2}{\theta_d^2}\right), \quad (\text{A3})$$

where  $\theta_d$  is diffusion radius, which is the only free parameter used for the model (Abeysekara et al. 2017). For the diffusion model, we have adopted the fixed parameters of Albert et al. (2022) used to model MGRO J1908+06, magnetic field of 3  $\mu\text{G}$  and diffusion coefficient spectral index of 1/3.  $\Delta\text{BIC}$  for the diffusion model compared to the Gaussian model is  $-50$  ( $= \text{BIC}_{\text{Diffusion}} - \text{BIC}_{\text{Gaussian}}$ ). Overall, the diffusion model best describes HAWC J1908+0618.

## B. SPECTRAL MODELS

Two spectral models (cutoff power-law and log parabola; COPL and LP) are tested for the found sources. The log parabola model is given by

$$\frac{dN}{dE_\gamma} = K \left( \frac{E_\gamma}{E_{\text{piv}}} \right)^{\alpha - \beta \log(E_\gamma/E_{\text{piv}})}, \quad (\text{B4})$$

where  $\beta$  is spectral curvature.

A cutoff power-law model is given by

$$\frac{dN}{dE_\gamma} = K \left( \frac{E_\gamma}{E_{\text{piv}}} \right)^\alpha \exp\left(-\frac{E_\gamma}{E_{\text{cutoff}}}\right), \quad (\text{B5})$$

where  $E_{\text{cutoff}}$  is cutoff energy. The spectrum decreases exponentially when the energy is greater than the cutoff energy. Only the spectrum of HAWC J1908+0618 is found to favour the LP model by  $\Delta\text{TS}_{\text{LP}} = 123$ . COPL and LP do not have distinct preferences over the simple power law model for other sources, including the two SS 433 jet lobes.

## C. ENERGY ESTIMATOR BINS

The values of flux points and upper limits presented in Figure 4 are tabulated in Table C1. The table also contains the energy range corresponding to each bin for the east and west SS 433 jet lobes.

## REFERENCES

- |   |   |
|---|---|
| <p>Abdo, A. A., Allen, B., Berley, D., et al. 2007, The Astrophysical Journal, 664, L91, doi: <a href="https://doi.org/10.1086/520717">10.1086/520717</a></p> <p>Abeysekara, A. U., Albert, A., Alfaro, R., et al. 2017, ApJ, 843, 39, doi: <a href="https://doi.org/10.3847/1538-4357/aa7555">10.3847/1538-4357/aa7555</a></p> <p><sup>3</sup> <i>astromodels</i>; <a href="https://github.com/threeML/astromodels">https://github.com/threeML/astromodels</a></p> | <p>Abeysekara, A. U., Albert, A., Alfaro, R., et al. 2017, The Astrophysical Journal, 843, 40, doi: <a href="https://doi.org/10.3847/1538-4357/aa7556">10.3847/1538-4357/aa7556</a></p> <p>Abeysekara, A. U., Albert, A., Alfaro, R., et al. 2017, Science, 358, 911, doi: <a href="https://doi.org/10.1126/science.aan4880">10.1126/science.aan4880</a></p> <p>Abeysekara, A. U., et al. 2018, Nature, 562, 82, doi: <a href="https://doi.org/10.1038/s41586-018-0565-5">10.1038/s41586-018-0565-5</a></p> |
|---|---|

Bins	Median [TeV]		Lower Bound [TeV]		Upper Bound [TeV]		$E^2 dN/dE$ [ $10^{-13}$ TeV cm $^{-2}$ s $^{-1}$ ]	
	west	east	west	east	west	east	west	east
c	1.1	1.1	0.6	0.6	1.9	1.8	48.6*	2210*
d	2.2	2.1	1.3	1.3	3.3	3.2	8.97*	9.01*
e	3.8	3.8	2.6	2.5	5.5	5.4	5.18*	10.7*
f	6.8	6.8	4.7	4.7	9.6	9.5	$2.65^{+0.99}_{-0.69}$	$2.47^{+0.92}_{-0.66}$
g	12.4	12.3	9.0	8.9	16.7	16.6	$1.95^{+0.73}_{-0.55}$	$2.07^{+0.65}_{-0.51}$
h	22.1	21.9	16.4	16.2	29.0	28.8	$1.33^{+0.58}_{-0.40}$	$1.27^{+0.52}_{-0.37}$
i	39.0	38.7	29.5	29.3	50.9	50.5	$2.12^{+0.57}_{-0.44}$	$1.11^{+0.49}_{-0.34}$
j	69.4	68.9	53.4	53.0	89.7	89.1	1.46*	1.16*
k	124.9	124.2	96.9	96.3	160.1	159.1	$0.851^{+0.655}_{-0.374}$	3.75*
l	218.7	217.2	169.4	168.3	287.5	285.4	425*	217*

**Table C1.** Energy bins and their corresponding median, lower bound (16% quantile), and upper bound (84% quantile) energies in TeV.  $E^2 dN/dE$  represents the best-fit flux while \* indicates upper limits. The upper limits are 90% confidence level.

- . 2019, *Astrophys. J.*, 881, 134, doi: [10.3847/1538-4357/ab2f7d](https://doi.org/10.3847/1538-4357/ab2f7d)
- . 2021, *PoS, ICRC2021*, 828, doi: [10.22323/1.395.0828](https://doi.org/10.22323/1.395.0828)
- Abeysekara, A. U., Albert, A., Alfaro, R., et al. 2023, *Nuclear Instruments and Methods in Physics Research A*, 1052, 168253, doi: [10.1016/j.nima.2023.168253](https://doi.org/10.1016/j.nima.2023.168253)
- Albert, A. ., Alfaro, R., Alvarez, C., et al. 2024, *Performance of the HAWC Observatory and TeV Gamma-Ray Measurements of the Crab Nebula with Improved Extensive Air Shower Reconstruction Algorithms.* <https://arxiv.org/abs/2405.06050>
- Albert, A., Alfaro, R., Alvarez, C., et al. 2022, *ApJ*, 928, 116, doi: [10.3847/1538-4357/ac56e5](https://doi.org/10.3847/1538-4357/ac56e5)
- Albert, A., et al. 2023, *PoS, ICRC2023*, 759, doi: [10.22323/1.444.0759](https://doi.org/10.22323/1.444.0759)
- Bartoli, B., Bernardini, P., Bi, X. J., et al. 2013, *ApJ*, 779, 27, doi: [10.1088/0004-637X/779/1/27](https://doi.org/10.1088/0004-637X/779/1/27)
- Brinkmann, W., Aschenbach, B., & Kawai, N. 1996, *A&A*, 312, 306
- Brinkmann, W., Pratt, G. W., Rohr, S., Kawai, N., & Burwitz, V. 2007, *A&A*, 463, 611, doi: [10.1051/0004-6361:20065570](https://doi.org/10.1051/0004-6361:20065570)
- Cao, Z., Aharonian, F. A., An, Q., et al. 2021, *Nature*, 594, 33, doi: [10.1038/s41586-021-03498-z](https://doi.org/10.1038/s41586-021-03498-z)
- Cao, Z., Aharonian, F., An, Q., et al. 2024, *ApJS*, 271, 25, doi: [10.3847/1538-4365/acfd29](https://doi.org/10.3847/1538-4365/acfd29)
- Fabrika, S. 2004, *Astrophys. Space Phys. Res.*, 12, 1, doi: [10.48550/arXiv.astro-ph/0603390](https://doi.org/10.48550/arXiv.astro-ph/0603390)
- Fang, K., Charles, E., & Blandford, R. D. 2020, *The Astrophysical Journal Letters*, 889, L5, doi: [10.3847/2041-8213/ab62b8](https://doi.org/10.3847/2041-8213/ab62b8)
- Geldzahler, B. J., Pauls, T., & Salter, C. J. 1980, *A&A*, 84, 237
- H. E. S. S. Collaboration, Olivera-Nieto, L., Reville, B., Hinton, J., & Tsirou, M. 2024, *Science*, 383, 402, doi: [10.1126/science.adi2048](https://doi.org/10.1126/science.adi2048)
- Kar, P. 2017, *PoS, ICRC2017*, 713, doi: [10.22323/1.301.0713](https://doi.org/10.22323/1.301.0713)
- Kass, R. E., & Raftery, A. E. 1995, *Journal of the American Statistical Association*, 90, 773, doi: [10.1080/01621459.1995.10476572](https://doi.org/10.1080/01621459.1995.10476572)
- Kimura, S. S., Murase, K., & Mészáros, P. 2020, *Astrophys. J.*, 904, 188, doi: [10.3847/1538-4357/abbe00](https://doi.org/10.3847/1538-4357/abbe00)
- Reynoso, M. M., & Carulli, A. M. 2019, *Astropart. Phys.*, 109, 25, doi: [10.1016/j.astropartphys.2019.02.003](https://doi.org/10.1016/j.astropartphys.2019.02.003)
- Safi-Harb, S., & Ögelman, H. 1997, *The Astrophysical Journal*, 483, 868, doi: [10.1086/304274](https://doi.org/10.1086/304274)
- Safi-Harb, S., & Petre, R. 1999, *The Astrophysical Journal*, 512, 784, doi: [10.1086/306803](https://doi.org/10.1086/306803)
- Safi-Harb, S., Intyre, B. M., Zhang, S., et al. 2022, *The Astrophysical Journal*, 935, 163, doi: [10.3847/1538-4357/ac7c05](https://doi.org/10.3847/1538-4357/ac7c05)
- Stephenson, C. B., & Sanduleak, N. 1977, *ApJS*, 33, 459, doi: [10.1086/190437](https://doi.org/10.1086/190437)
- Sudoh, T., Inoue, Y., & Khangulyan, D. 2020, *ApJ*, 889, 146, doi: [10.3847/1538-4357/ab6442](https://doi.org/10.3847/1538-4357/ab6442)
- Vianello, G., Lauer, R. J., Younk, P., et al. 2015, *The Multi-Mission Maximum Likelihood framework (3ML)*, arXiv, doi: [10.48550/ARXIV.1507.08343](https://doi.org/10.48550/ARXIV.1507.08343)
- Wakely, S. P., & Horan, D. 2008, *International Cosmic Ray Conference*, 3, 1341
- Wilks, S. S. 1938, *The Annals of Mathematical Statistics*, 9, 60, doi: [10.1214/aoms/1177732360](https://doi.org/10.1214/aoms/1177732360)